Crystal Structures of Human Prostatic Acid Phosphatase in Complex with a Phosphate Ion and α-Benzylaminobenzylphosphonic Acid Update the Mechanistic Picture and Offer New Insights into Inhibitor Design[†,‡]

Eric Ortlund, Michael W. LaCount, and Lukasz Lebioda*

Department of Chemistry and Biochemistry, University of South Carolina, Columbia, South Carolina 29208

Received July 24, 2002; Revised Manuscript Received November 1, 2002

ABSTRACT: The X-ray crystal structure of human prostatic acid phosphatase (PAP) in complex with a phosphate ion has been determined at 2.4 Å resolution. This structure offers a snapshot of the final intermediate in the catalytic mechanism and does not support the role of Asp 258 as a proton donor in catalysis. A total of eight hydrogen bonds serve to strongly bind the phosphate ion within the active site. Bound PEG molecules from the crystallization matrix have allowed the identification of a channel within the molecule that likely plays a role in molecular recognition and in macromolecular substrate selectivity. Additionally, the structure of PAP in complex with a phosphate derivative, α-benzylaminobenzylphosphonic acid, a potent inhibitor (IC_{50} = 4 nM), has been determined to 2.9 Å resolution. This structure gives new insight into the determinants of binding hydrophobic ligands within the active site and allows us to explain PAP's preference for aromatic substrates.

Human prostatic acid phosphatase, discovered in 1935 by Kutcher and Wolberg, has been of significant medical interest ever since tests screening for serum PAP levels were introduced to diagnose and stage prostate cancer (*1*). Recently, the primary diagnostic protocol for detecting prostate cancer has shifted from evaluating serum PAP levels to utilizing the prostate specific antigen (PSA) test. The accurate measurement of serum PAP levels is still of considerable interest, however, due to its effectiveness in staging metastatic prostatic cancer and evaluating the progress of chemotherapy in cancer patients (*2*).

Protein tyrosine kinases (PTKs)[1] play an important role in the normal and malignant growth of cells (*3*) and have been extensively studied for nearly two decades. In contrast, relatively little is known about the functional role of protein tyrosine phosphatases (PTPs). Only recently have PTPs studies intensified as their importance in maintaining controlled cellular growth and possibly oncogenesis has been explored (*4*−*8*).

PAP has been shown to possess protein tyrosine phosphatase activity as demonstrated in vitro by its ability to dephosphorylate the EGF receptor from prostate carcinoma cells (*7*), but its physiological substrate remains unknown. It has been demonstrated that human prostate cancer cells show a decreased level of expression of the cellular form of the enzyme and that the intracellular level of this enzyme is inversely correlated with the cellular growth rate (*8*−*11*).

PAP, which is secreted by epithelial cells in the prostate gland, is found in seminal fluid at concentrations reaching 1 mg/mL (*12*). PAP belongs to the family of high-molecular mass phosphatases and is classified as an acid phosphatase due to its optimum pH range of 4−7. Mature PAP is secreted as a glycosylated homodimer consisting of two 50 kDa subunits. The enzyme is capable of hydrolyzing a wide spectrum of substrates, including alkyl, aryl, and orthophosphate monoesters in addition to phosphotyrosyl proteins (*13*). Human PAP, like most phosphomonoesterases, is also able to catalyze the transfer of phosphoryl groups to hydroxyl compounds (*14*).

The catalytic mechanism of the enzyme has been extensively studied, including numerous mechanistic studies, and it was concluded that PAP acts like a histidine phosphatase (*15*−*17*). Site-directed mutagenesis studies have shown that H12 and R11 are essential for catalysis, while substitution of residues corresponding to R15, R79, H257, and D258 severely impairs catalytic activity (*18*). The crystal structures of complexes of the rat enzyme with vanadate and molybdate ions have also been reported (*19*); the active site residues are conserved between rat and human PAP, and these studies appear to be applicable to the human enzyme. The structures show the ions forming covalent bonds to the active site H12; therefore, they represent an important reaction intermediate. The metal atoms are pentacoordinated with trigonal bipyramidal geometry. These and other studies have allowed for a detailed mechanistic description of the catalytic process (*17*, *19*, *20*). The reaction proceeds via the classic double-displacement pathway in accordance with Scheme 1 (*20*). The reaction is initiated by the attack of the active site H12

[†] This research was supported in part by National Institutes of Health Grant NIH GM42898. Some instrumentation used in this research was purchased with NSF Grant BIR 9419866 and DOE Grant DE-FG-95TE00058.

[‡] The coordinates have been deposited with the Protein Data Bank as entries 1ND6 and 1ND5.

* To whom correspondence should be addressed. Phone: 01 (803) 777-2140. Fax: 01 (803) 777-9521. E-mail: Lebioda@mail.chem.sc.edu.

[1] Abbreviations: PAP, human prostatic acid phosphatase; rPAP, rat prostatic acid phosphatase; PTK, protein tyrosine kinase; EGF, epidermal growth factor; PEG, poly(ethylene glycol); BABPA, α-benzylaminobenzylphosphonic acid.

10.1021/bi0265067 CCC: $25.00
Published on Web 12/21/2002

Scheme 1

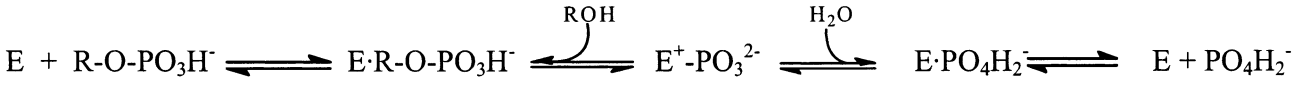

on the phosphate ester, resulting in a phosphoramidate intermediate with release of the alcohol. The rate-limiting step is the breakdown of this intermediate via the addition of a nucleophilic water molecule, most likely activated by D258, liberating inorganic phosphate and the free enzyme. The result is a noncovalent binary enzyme−inorganic phosphate complex, which dissociates, readying the enzyme for the next substrate.

Recently determined structures of bacterial phosphatases [phytase from *Escherichia coli* (*21*), phytase from *Aspergillus niger* (*22*), and pH 2.5 acid phosphatase from *A. niger* (*23*)] revealed structural and mechanistic similarity to PAP, implying distant homology.

Unexpectedly, recent studies have shown strong expression of PAP by breast cancer cells (*24*) and elevated levels of PAP in tumors of neuroendocrine origin (*25*). Whether this phenomenon gives an advantage to proliferating cells or is just an aberration of cancer biology remains an open question. PAP specific inhibitors should be a valuable tool for studies of this problem. To this end, we have engaged in structure-based development of tartrate-related PAP inhibitors; preliminary data are reported elsewhere (*26*). Here we report the structures of complexes of PAP with a phosphate ion and with a phosphate-based inhibitor. The former is the most precise structure of a eukaryotic histidine phosphatase reported yet.

MATERIALS AND METHODS

Human PAP was purified from semen using tartrate affinity chromatography as previously described by Van Etten (*27*). Crystals were grown from solutions containing 7−10 mg of protein/mL, 30% PEG 1500, 7% PEG 1000, 6% PEG 400, 100 mM KCl, and 100 mM glycine (pH 10.0). Typical crystals grew to a size of 0.15 mm × 0.1 mm × 0.1 mm and were then used in a macroseeding procedure that yielded crystals with dimensions of 0.2 mm × 0.15 mm × 0.15 mm. These crystals belong to space group $P2_12_12_1$ with the following unit cell dimensions: $a = 119.89$ Å, $b = 203.32$ Å, and $c = 79.89$ Å. The crystals were then soaked in an artificial mother liquor solution containing either sodium thymolphthalein monophosphate or α-benzylaminobenzylphosphonic acid (BABPA) for 2 days prior to data collection. Thymolphthalein monophosphate was purchased from Sigma, and BABPA was a gift from Johnson & Johnson Pharmaceuticals.

The soaked crystals were flash-frozen at 123 K in a stream of nitrogen generated by a low-temperature X-Stream attachment (Molecular Structure Corp.). A Rigaku rotating anode source at 50 kV and 100 mA with mirror optics and a Raxis IV area detector at a distance of 170 mm were used to collect data as 1° oscillation frames over a 180° range. After rejection of reflections for which $I < 1\sigma(I)$, the data set for the PAP·P_i complex is 99.5% complete to 2.4 Å resolution (99.8% in the 2.47−2.36 Å shell) with 89 003 unique reflections and an R_{merge} of 5.6%. After rejection of reflections for which $I < 1\sigma(I)$, the data set for the PAP·BABPA complex is 82.2% complete to 2.9 Å resolution (68.9% in the 3.00−2.89 Å shell) with 33 191 unique reflections and an R_{merge} of 6.3%. All data were processed with the HKL suite of programs (*28*).

Table 1: Data Collection and Refinement Statistics

	PO_4 complex	PABA complex
resolution (Å)	50−2.4	50−2.9
no. of reflections	89003	33191
R_{merge} (%)	5.6	6.3
completeness (%) (last shell)	99.5 [99.8 (2.47−2.36 Å)]	82.2 [63.7 (3.0−2.89 Å)]
no. of waters	464	136
no. of carbohydrate atoms	267	180
no. of PEG atoms	108	127
no. of PO_4 or PABA atoms	20	76
$R_{working}/R_{free}$ (%)	18.8/25.2	20.2/27.8
rms deviations		
bonds (Å)	0.006	0.007
angles (deg)	1.3	1.3

Molecular Modeling and Refinement. Initial phases were obtained from the crystal structure of native human PAP determined at 3.1 Å resolution at room temperature (*29*). The structure was optimized using simulated annealing, conjugate gradient minimization, and *B*-factor refinements with the CNS software (*30*). Visual inspection of the maps and model rebuilding were carried out with Turbo Frodo (*31*). A phosphate ion was then manually fitted in the corresponding $F_o - F_c$ density in all four subunits of the PAP·P_i complex. The *R* factor of the final model is 19.1% ($R_{free} = 25.5\%$) in the resolution range of 12−2.4 Å with a root-mean-square deviation from ideal bond lengths of 0.006 Å and bond angles of 1.3°. Similarly, BABPA was modeled into the corresponding $F_o - F_c$ density present again in all four subunits of the PAP·BABPA complex. The final model yielded an *R* of 20.2% ($R_{free} = 27.8\%$) in the resolution range of 12−2.9 Å (Table 1). Superpositions were performed with LSQKAB and TOP from the CCP4 suite of programs (*32*). Accessible surface area calculations were performed with the Lee and Richards buried surface accessibility algorithm in CNS using a 1.4 Å probe radius. Two dimers (A−B and C−D) are present in the asymmetric part of the unit cell, but the quality of the data was such that noncrystallographic symmetry restraints were not used during the refinement.

RESULTS

Phosphate Binding. Electron density maps are excellent in general and reflect the highest-resolution data collected for PAP to date. In particular, the active site density is very good, allowing for unambiguous positioning of the HPO_4^{2-} ion. In all four subunits comprising the asymmetric unit, there is tetrahedral electron density characteristic for a phosphate ion (Figure 1). It is apparent that despite the high pH of the mother liquor the substrate, thymolphthalein monophosphate, was hydrolyzed and the alcohol product has dissociated. The center of the tetrahedral electron density is 3.0 Å from H12, too far to represent a P−N covalent bond. The positions of the four phosphate oxygen atoms are clearly depicted by the tetrahedral density and are coordinated by residues R11, H12,

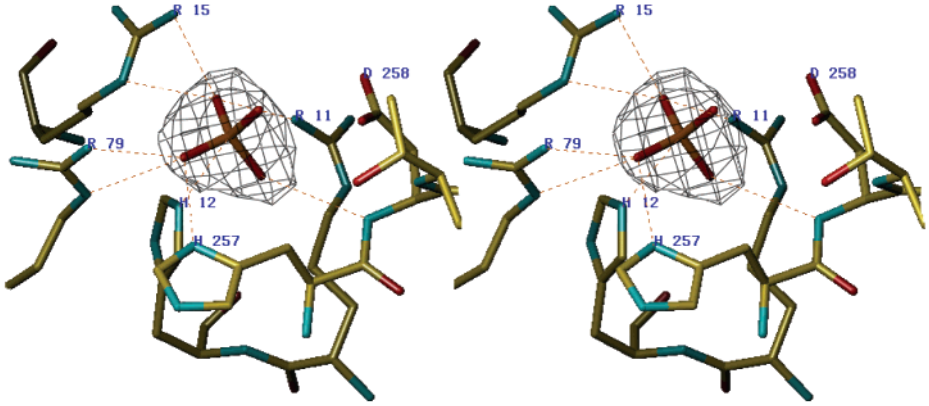

FIGURE 1: In all four monomers comprising the asymmetric unit, there is tetrahedral electron density characteristic of a phosphate ion. It is apparent that despite the high pH, the substrate was hydrolyzed and the alcohol has dissociated. The phosphate atom at the center of the density is located 3 Å from His12, too far to represent a covalent bond. The positions of the four phosphate oxygen atoms are clearly reflected in the tetrahedral density and are coordinated by residues Arg11, His12, Arg15, Arg79, His257, and Asp258 forming a total of eight hydrogen bonds.

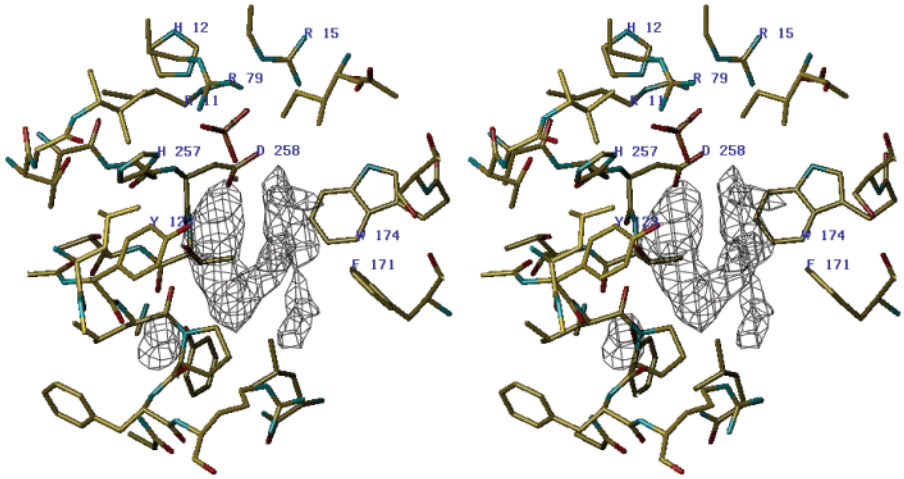

FIGURE 2: $F_o - F_c$ density located in the opening of the active site pocket for monomer D in the asymmetric unit. It is tubular in shape and is situated approximately 2.8 Å from the face of the aromatic ring of Y123. This density is located approximately 3 Å from the phosphate moiety and extends toward the opening of the active site. The density appears to be too large in diameter to represent PEG alone and likely corresponds to the partial occupancy of both thymolphthalein and PEG.

R15, R79, H257, and D258. Three oxygen atoms of the phosphate ion are positioned so that they are equidistant from NE2 of H12, supporting the theory of an axial attack by this nucleophile (*19*).

Additional density, not corresponding to water molecules, is observed in the active sites of all four subunits. This density is located approximately 3 Å from the phosphate moiety and extends toward the opening of the active site (Figure 2). It is tubular in shape and is situated approximately 2.8 Å from the face of the aromatic ring of Y123. This density is much stronger in subunit D than in the other three subunits, and extends to form a van der Waals contact with Phe171. Sodium thymolphthalein monophosphate, a highly specific substrate for PAP versus other phosphatases (*33*), was used for the soaking experiment; however, the resulting alcohol could not be modeled into this density with certainty. Thus, no ligand was assigned to this density during the refinement. It is possible that this density represents the multiple binding modes of thymolphthalein as this region of the active site presents multiple sites for hydrophobic contacts. The enzyme has a higher affinity for aromatic substrates, and tartrate-based inhibitors that possess such aromatic groups exhibit significantly tighter binding than does tartrate ion alone (*34*). Thus, it is likely that this density represents a mixture of bound thymolphthalein and/or PEG present in the mother liquor.

PEG Pentamer Density in the PAP·P_i Complex. Strong density was observed in $F_o - F_c$ maps in the cavity formed by W336 and a stretch of residues S117−Q128 near the dimer interface. The density was continuous, tubular, and of a length corresponding to approximately five poly(ethylene glycol) repeats. The modeled PEG pentamer is in contact with the side chains of three residues (W336, Q120, and N128) and is within 7 Å of the corresponding PEG pentamer modeled into the neighboring subunit (Figure 3). The PEG density is located close to the 2-fold symmetry axis at the dimer interface in the proximity of the active site cleft. This region of the dimer is convex, forming a trough roughly 20 Å wide allowing access to both active site clefts. Also noteworthy is the existence of a channel ~10 Å in length that connects the extra density within the active site, presumably corresponding to partially present thymolphthalein or PEG, to the PEG pentamer density. This portion of the enzyme may serve to aid in the recognition of protein substrates.

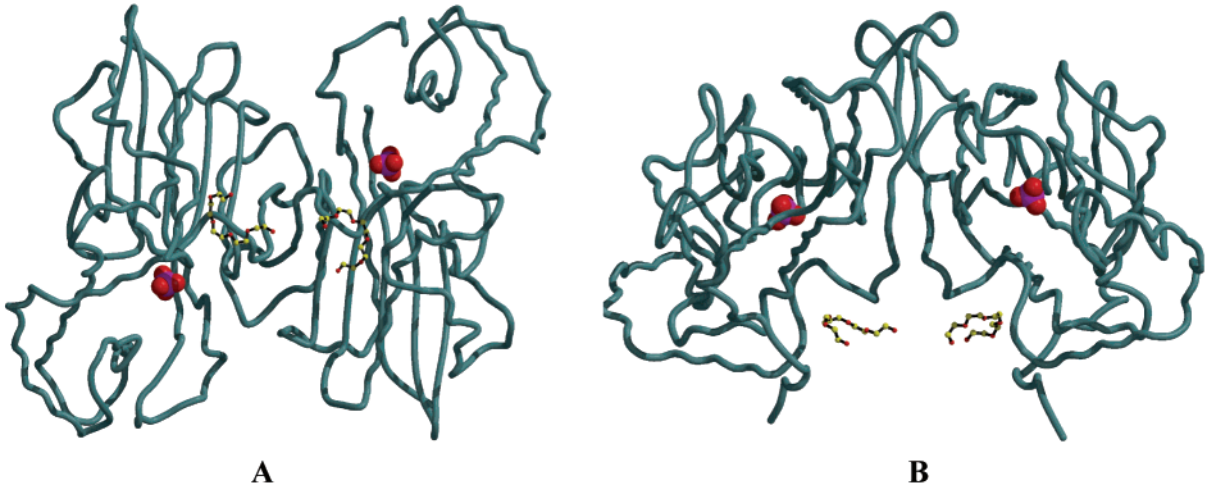

FIGURE 3: (A) View of the PAP dimer looking down the 2-fold axis. Phosphate ions are rendered as space filing models, and the PEG pentamers are rendered as balls and sticks. Carbon atoms are yellow and oxygen atoms red. This view shows the proximity of the PEG molecules to the active site. The PEG pentamers are 7 Å apart and roughly 10 Å from the active site. (B) View of the PAP dimer perpendicular to the 2-fold axis. This region of the dimer is convex, forming a trough roughly 20 Å wide allowing access to both active site clefts.

Carbohydrates. Initial coordinates that describe in detail the composition and position of the N-linked oligosaccharide chains were based on the structure of the native enzyme (*29*). These coordinates were based on 3.1 Å resolution data and were found to be essentially correct. Surprisingly, carbohydrate density for several of the oligosaccharide units was weak, indicating more disorder than was observed in the native crystal. This led to the removal of several terminal carbohydrate moieties. On the other hand, for two glycosylation sites (N301 of subunit B and subunit D of the respective dimers) density was improved, justifying the placement of additional carbohydrate residues.

Tetramer Interface. PAP is active as a strongly bound dimer; denaturation−renaturation and subunit reassociation experiments showed that the PAP activity depends on dimer formation (*35*). Subsequently, it was proposed that formation of the dimer is instrumental in positioning R79 in the active site (*36*). The catalytic importance of this residue was demonstrated in both the human and rat enzymes as the R79A mutant showed little or no catalytic activity (*18*, *19*). Recently, the steady state kinetics of the PAP were reevaluated, and PAP was found to exhibit positive cooperativity toward the three substrates that were studied: 1-naphthyl phosphate, phenyl phosphate, and phosphotyrosine (*11*). Cooperativity was dependent on both the aromatic nature of the ligand and the concentration of phosphatase. Interestingly, as the concentration of PAP was increased, the observed cooperativity also increased as evidenced by an increase in the calculated Hill cooperation coefficient. For instance, the Hill coefficient observed for 1-naphthyl phosphate increased from 1.66 to 3.59 when the PAP concentration was increased from 2.1 to 68.1 nM. Since the Hill coefficient cannot exceed the number of enzyme subunits, these data lead Luchter-Wasylewska to propose that the active species is a dimer, tetramer, or oligomer depending on the protein concentration (*11*).

The rPAP crystals contain one subunit in the asymmetric part of the unit cell; the active dimer is generated by a crystallographic 2-fold axis, and all other symmetry elements contain a translational component (*19*). This is not consistent with the formation of tetramers by rPAP. The asymmetric part of the unit cell in the human enzyme crystals contains two dimers that show a fairly strong interaction with each other. The formation of the active dimer from two monomers leads to a reduction of the accessible surface from 32 091 to 29 195 Å^2, a difference of 2896 Å^2 or approximately 10% of the total accessible surface. Hypothetical tetramer (dimer−dimer) formation as observed in the crystal leads to a reduction of accessible surface from 58 171 to 55 614 Å^2. This yields a difference of 2556 Å^2, corresponding to a 5% reduction in the total accessible surface. Even more importantly, the tetramer interface is significantly more hydrophilic than the dimer interface as evidenced by formation of 11 interdimer hydrogen bonds. The main interaction between the dimers occurs at the open face of the active site cleft with the opening of the active site cleft in subunit A positioned directly over the corresponding active site in subunit D. This leads to a linear association of dimers whereby the corresponding positions of dimer−dimer interactions in both subunits B and C appear to be free to associate with other dimers. In fact, visualization of symmetrically equivalent atoms within the unit cell reveals that the dimers indeed associate in the same manner with the available sites on subunits B and C. This arrangement of subunits serves to partially block substrate access to two of the active sites within the tetramer. As evidenced by the structures reported here and the isomorphous PAP−*N*-propyl tartramate complex (*34*), small substrates easily gain access to the buried active sites; however, large substrates such at tyrosyl proteins would certainly be precluded. This evidence, coupled with the fact that the dimer−dimer interface is predominantly hydrophilic, suggests that the observed tetrameric arrangement is not significantly populated in solution.

BABPA Binding. Despite the lower-resolution data, density corresponding to the BABPA molecule and the active site residues is quite good. This has been observed previously in PAP complexes and is presumably due to high order within the active site region. The phosphono group is anchored by the same positively charged residues shown to coordinate phosphate ion in the PAP·P_i complex (Figure 4). The carboxylate of D258 remains within 3 Å of the phosphonic carbon; however, the inhibitor is oriented in such

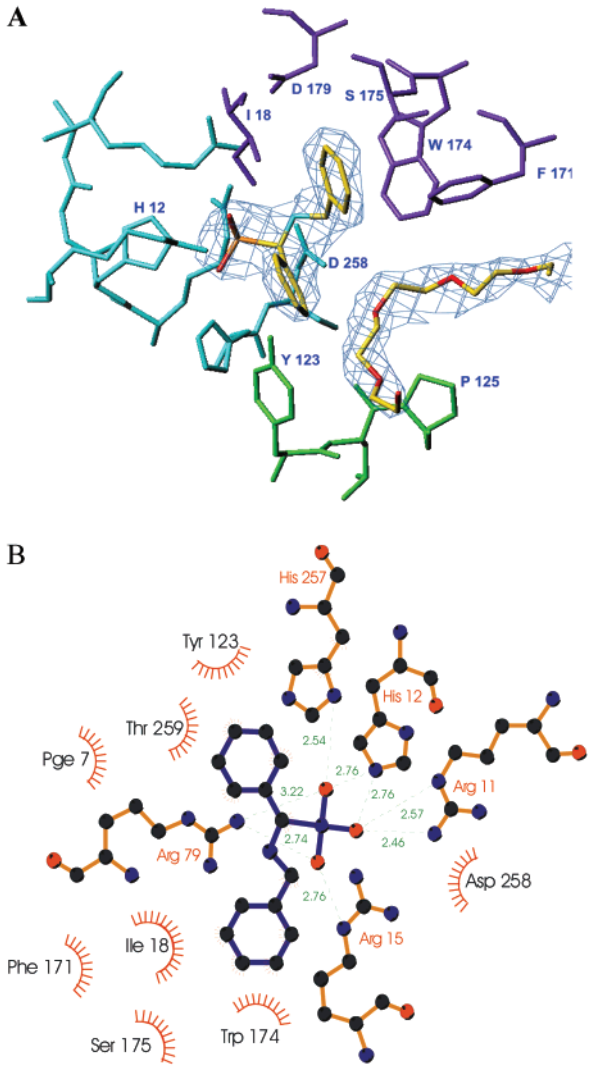

FIGURE 4: (A) $2F_o - F_c$ density within the active site of the PAP·BABPA complex contoured at 1σ. Density for the bound BABPA inhibitor is present in all four subunits along with tubular density corresponding to approximately five PEG repeats. The phosphono group is anchored by the same positively charged residues (cyan) shown to coordinate the phosphate ion in the PAP·PO_4^{2-} complex. As with the PAP·PO_4^{2-} complex, the phosphate atom is ~3 Å from the NE2 atom of His12, indicating a noncovalent interaction. Residues within van der Waals distance of the benzylamino group are shown in purple and form a relatively hydrophobic binding site with the exception of Asp179. The carboxylate of this residue is ~4.5 Å from the benzyl moiety and is approximately perpendicular to the plane of the ring. Residues Tyr123 and Pro125 (green) are part of a more open channel that interacts with both the PEG molecule and the benzyl group of the inhibitor. (B) Ligplot drawing showing in detail the specific interactions of BABPA with the active site (*39*).

a way that H-bonding between the nitrogen of the benzylamino moiety and the carboxylate of D258 is not present. The benzylamino group of the inhibitor is within van der Waals distance of I18, F171, W174, and S175, taking advantage of a distinct hydrophobic binding pocket within the active site (Figure 4). D179 is not a part of the aforementioned hydrophobic pocket as it remains out of van der Waals contact (~4.5 Å) with the aminobenzyl group. Previous studies by Beers et al. (*37*) showed that the addition of a hydroxyl group at the 2 or 3 position of this aminobenzyl moiety slightly improved the IC_{50} for the inhibitor. Such a H-bond donor would be well positioned to interact with this

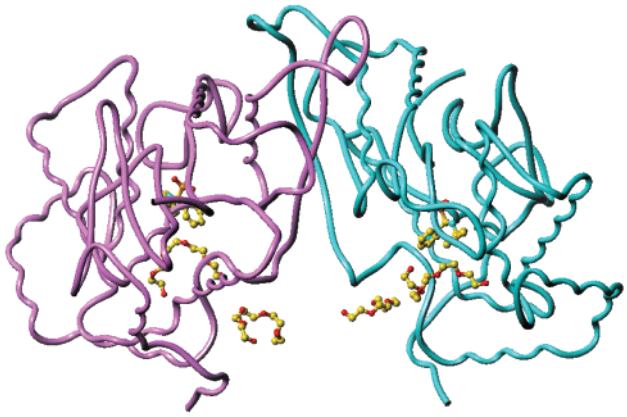

FIGURE 5: PAP dimer rendered as a coil with the BABPA inhibitor and PEG molecules rendered as balls and sticks. This is a general view that allows one to see locations of the PEG molecules as they fill the channel connecting the active site to the trough located near the dimer interface.

residue and is likely the reason for the increased level of binding. Beers et al. (*37*) also noted another slight improvement in the IC_{50} value upon the addition of methyl group at the 3 position on the benzyl moiety. The carbon at the 3 position on this aromatic ring is 3.7 Å away from the Y123 hydroxyl. A slight shift in the position of the Y123 side chain could easily accommodate the added methyl group while maintaining a suitable stabilizing interaction.

Tubular density corresponding to approximately five poly(ethylene glycol) repeats is also present within the entrance to the active site in each subunit. This density is situated in a channel linking the active site with the PEG molecules located in the trough at the dimer interface (Figure 5).

DISCUSSION

The structure of the PAP·P_i complex represents the enzyme−product complex, adding another view to the mechanistic picture of PAP. A superposition of the human PAP·P_i complex (pH 10.0) on the rat PAP−vanadate complex (pH 5.4) and *E. coli* phytase−tungstate (pH 6.6) complex reveals high-level conservation of the positions of all active site residues aside from some minor deviation in the conformation of residue R79 (Figure 6). The structure of the PAP·P_i complex strongly supports the theory of an axial attack by H12, as three oxygen atoms of the phosphate ion are positioned such that they are equidistant from the H12 NE2 atom. The phosphate ion is coordinated by active site residues R11, R15, R79, and H257 and overneutralized by four positive charges. The resulting polarization depletes the electron density at the phosphorus atom, readying it for nucleophilic attack by H12.

Our data corroborate the roles of active site residues in the reaction mechanism proposed by Lindqvist et al. (*19*); however, some details should be reconsidered. At the enzyme's optimum pH, the substrate most likely enters the active site carrying one proton. It is less certain if H257 is protonated due to its proximity to R79, but protonation of this residue is likely. Certainly in the PAP·P_i complex, there is a hydrogen bond between H257 and the phosphate ion. The pK_a values for the phosphoric acid and histidinium moiety are similar, but with the oxygen atom of the phosphate moiety being the acceptor of two hydrogen bonds from the guanidinium group of R79 (Figure 1), it appears

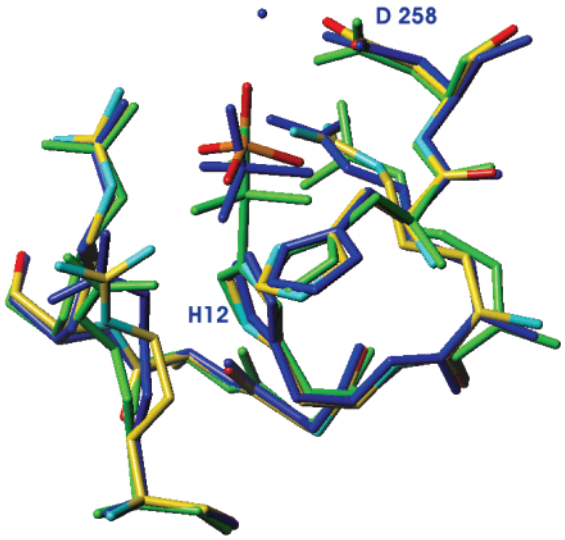

FIGURE 6: Superposition of the rat PAP−vanadate complex (green, pH 5.4) and the *E. coli* phytase−tungstenate complex (blue, pH 6.6) on the human PAP·P_i complex (standard atomic colors, pH 10.0). The positions of the active site residues between these two complexes are highly similar. Vanadate is covalently bound to H12, while the phosphate and tungstate ion are not. The orientation of the putative general acid catalyst, D258 (D258 in rat PAP and D403 in phytase), is nearly identical in all three structures.

more likely that the proton resides on H257. It is also likely that D258 remains in the deprotonated form at the physiological pH and the enzyme's optimum pH of 5.0 as the pK_a of aspartic acid in polypeptide chains is normally 3.8−4.0. In PAP, the pK_a of D258 is presumably lower since its carboxyl group is 3.2 Å from the guanidinium moiety of R11. In the PAP·P_i complex, the distance between the axial oxygen atom of the phosphate moiety and the carboxylate group of D258 is 2.8 Å, suggesting the formation of a hydrogen bond as two acidic oxygen atoms tend to form a site favoring proton binding. The geometry of this arrangement, however, strongly suggests that if indeed such a H-bond is formed the proton resides on the phosphate ion (see Figure 1). The directions of the sp^2 orbitals of the D258 carboxylate group, which would have to form the covalent O−H bond, point above the axial oxygen atom. Thus, to have an effective proton transfer to the carboxylate of D258 and formation of an H-bond in which an oxygen atom of the carboxylate serves as the donor, a rotation of this side chain would be required. Proton transfer from the carboxylate of D258 to the alcohol leaving group has been previously postulated in the PAP mechanism (*19*). This transfer is not crucial since a plausible alternative is that the carboxylate simply facilitates an intramolecular proton jump from an equatorial oxygen atom to the axial oxygen atom within the phosphate moiety upon the entrance of the phosphate ester into the binding pocket. This transforms the alkoxy portion of the phosphoester into a good leaving group. Even more importantly, D258 was postulated to play a role in the activation of a water molecule that attacks the phosphoramidate intermediate; being happily hydrogen bonded to the phosphate moiety certainly would not facilitate such a function. In the rat PAP−vanadate complex, the position of D258 in carboxylate is essentially the same as in the PAP·P_i complex (Figure 6) and similarly is not consistent with this residue functioning as a hydrogen bond donor to an oxygen of the vanadate [the vanadate complex structure does not report solvent (*19*), and thus, the position of the water molecule that is likely to attack the covalent intermediate cannot be verified]. The ability of D258 to bind a water molecule in a position suitable for nucleophilic attack on the phosphohistidine intermediate is clearly demonstrated in the *E. coli* phytase−tungstate complex (Figure 6) where D304 (equivalent to D258) has coordinated a water molecule in a position just above the tungstate ion. It is likely that D258 in PAP serves to polarize the water molecule and facilitates its nucleophilic attack on the phosphohistidine intermediate. Importantly, the structure of the rat PAP−vanadate complex was determined at pH 5.4, close to the enzyme's optimum, and the structure of the *E. coli* phytase−tungstate complex was determined at pH 6.6. The position of the D258 side chain is thus not dependent on pH (or reaction state), and the structure of the PAP·P_i complex is very likely similar at more acidic pH values (Figure 6). Studies on *E. coli* acid phosphatase in which D304 (D258 in PAP) was mutated to an alanine or glutamic acid showed that these modifications lead to a greatly reduced V_{max} without markedly changing K_m (*20*). Additionally, these experiments showed that in the D304A (D258 in PAP) mutant the formation of the phosphohistidine intermediate becomes the rate-limiting step and that the activity of the mutant was highly dependent on the pK_a of the leaving alcohol. Thus, it was concluded that this residue plays a critical role in the protonation of the alcohol leaving group. These data are in agreement with previous studies of ratPAP

Scheme 2[a]

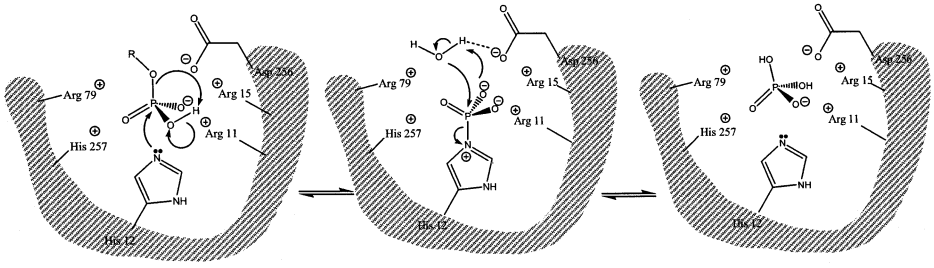

[a] As the phosphate ester enters the active site, Asp258 facilitates the migration of the phosphate proton from an equatorial oxygen to the axial oxygen atom of the phosphate moiety, creating a dianion which is coordinated by four cationic residues (Arg11, Arg15, Arg79, and His257) which serve to depolarize the substrate. Nucleophilic attack of His12 results in a phosphoramidite intermediate releasing the corresponding alcohol. The rate-limiting step is the breakdown of this intermediate through the addition of a nucleophilic water molecule, most likely activated by Asp258, to the phosphohistidine via an S_N2 mechanism. The resultant noncovalent binary enzyme−inorganic phosphate complex may then dissociate, readying the enzyme for the next substrate.

which also showed a reduced V_{max} and a decreased K_m for the D258A mutant (*36*). The decreased K_m in the alanine mutants, which cannot form a hydrogen bond, indicates that there is no hydrogen bonding between a substrate molecule and D258 in the Michaelis complex and that D258 plays a role in the later stages of the reaction.

The PAP mechanism is summarized in Scheme 2.

A superposition of the structures of the vanadate and phosphate complexes (Figure 6), the covalent and noncovalent intermediates in the catalytic mechanism, also offers an interesting glimpse at enzyme dynamics during catalysis. It is apparent that it is the oxoanion (or the substrate molecule), not the imidazole of H12, that moves relative to the protein frame during the formation of a covalent bond between the nitrogen and phosphorus atoms. At first, this appears to be counterintuitive because this movement requires adjustment of all interactions between the substrate and the enzyme. However, this is apparently favorable, requiring very little if any adjustment of the protein main chain during this step as evidenced by the high level of similarity of the covalent and noncovalent complexes.

BABPA is a potent PAP inhibitor (IC_{50} = 4 nM) as it combines phosphate binding with favorable hydrophobic interactions within the active site. Although the specificity of this inhibitor has not been tested on other phosphatases, it is thought that phosphate-derived inhibitors would not exhibit high specificity, considering that vanadates and molybdates are general phosphatase inhibitors and other aromatic derivatives of phosphonic acid inhibit nonhomologous tyrosine phosphatases (*38*). The structure of this complex does, however, reveal key information for the improvement of PAP specific inhibitors such as tartrate-based derivatives. Future inhibitors will need to take advantage of the hydrophobic pocket created by residues I18, F171, W174, and S175 and would ideally contain a means of interacting with D129 through hydrogen bonding. Improved inhibitors should interact with Y123 and take advantage of the channel linking the active site with the trough located near the dimer interface. Perhaps a simple PEG-ylation of the benzyl moiety would accomplish this task. The specific inhibitors of PAP should be effective tools in the search for the physiological substrate of PAP and may find applications in cancer diagnostics or therapy. The structure of the PAP·BABPA complex is a stepping stone toward the design of such inhibitors.

REFERENCES

1. Gutman, E. B., Sproul, E. E., and Gutman, A. B. (1936) *Am. J. Cancer 28*, 485−496.
2. Shetty, S. D., and Cerny, J. C. (1992) *Henry Ford Hosp. Med. J. 40*, 93−98.
3. Bishop, J. M. (1983) *Annu. Rev. Biochem. 52*, 301−345.
4. Lu, Z., Jiang, G., Blume-Jensen, P., and Hunter, T. (2001) *Mol. Cell. Biol. 21*, 4016−4031.
5. Mustelin, T., Brockdorff, J., Gjörloff-Wingren, A., Tailor, P., Han, S., Wang, X., and Saxena, M. (1998) *Front. Biosci. 3*, 1060−1096.
6. Saha, S., Bardelli, A., Buckhaults, P., Velculescu, V. E., Rago, C., St. Croix, B., Romans, K. E., Choti, M. A., Lengauer, C., Kinzler, K. W., and Vogelstein, B. (2001) *Science 294*, 1343−1346.
7. Lin, M., and Clinton, M. (1986) *Biochem. J. 235*, 351−357.
8. Lin, M. F., Lee, M. S., Zhou, X. W., Andressen, J., Meng, T. Z., Johansson, S., West, W. W., Taylor, R., Anderson, J., and Lin, F. F. (2001) *J. Urol. 166*, 1943−1950.
9. Meng, T. C., and Lin, M. F. (2000) *J. Biol. Chem. 273*, 22096−22104.
10. Zhang, X. Q., Lee, M. S., Zelivianski, S., and Lin, M. F. (2001) *J. Biol. Chem. 276*, 2544−2550.
11. Luchter-Wasylewska, E. (2001) *Biochim. Biophys. Acta 1548*, 257−264.
12. Rönnberg, L., Vihko, P., Sajanti, E., and Vihko, R. (1981) *Int. J. Androl. 4*, 372−378.
13. Apostol, I., Kuciel, R., Wasylewska, E., and Ostrowski, W. (1985) *Acta Biochim. Pol. 32*, 187−197.
14. Ostrowski, W., and Barnard, E. A. (1971) *Biochim. Biophys. Acta 250*, 131−142.
15. Ostrowski, W. (1978) *Biochim. Biophys. Acta 526*, 147−153.
16. Buchwald, S. L., Saini, S. M., Knowles, J. R., and Van Etten, R. L. (1984) *J. Biol. Chem. 259*, 2208−2213.
17. Van Etten, R. L. (1982) *Ann. N.Y. Acad. Sci. 390*, 27.
18. Ostanin, K., Saeed, A., and Van Etten, R. L. (1994) *J. Biol. Chem. 269*, 8971−8978.
19. Lindqvist, Y., Schneider, G., and Vihko, P. (1994) *Eur. J. Biochem. 221*, 139−142.
20. Ostanin, K., and Van Etten, R. L. (1993) *J. Biol. Chem. 268*, 20778−20784.
21. Lim, D., Golovan, S., Forsberg, C. W., and Jai, Z. (2000) *Nat. Struct. Biol. 7*, 108−113.
22. Kostrewa, D., Grüninger-Leitch, F., D'Arcy, A., Broger, C., Mitchell, D., and van Loon, A. P. G. M. (1997) *Nat. Struct. Biol. 4*, 185−190.
23. Kostrewa, D., Wyss, M., D'Arcy, A., and van Loon, A. P. G. M. (1999) *J. Mol. Biol. 288*, 965−974.
24. http://cgap.nci.nih.gov/Tissues/VirtualNorthern?TEXT=0andORG=HsandCID=1852.
25. Kaneko, Y., Motoi, A., Matsui, A., Motoi, T., Oka, T., Machinami, R., and Kurokawa, K. (1995) *Intern. Med. 34*, 886−891.
26. Ortlund, E. A. (2002) Crystallographic and Biochemical Studies of *Pseudomonas* 7A Glutaminase-Asparaginase, Human Prostatic Acid Phosphatase, Human Complement C8γ and Chicken Annexin V, Ph.D. Dissertation, pp 131−152, University of South Carolina, Columbia, SC.
27. Van Etten, R. L., and Saini, M. S. (1978) *Clin. Chem. 24*, 1520−1530.
28. Otwinowski, Z., and Minor, W. (1997) *Methods Enzymol. 276*, 307−326.
29. Jakob, C. G., Lewinski, K., Kuciel, R., Ostrowski, W., and Lebioda, L. (2000) *Prostate 42*, 211−218.
30. Brunger, A. T., Adams, P. D., Clore, G. M., Delano, W. L., Gros, P., Grosse-Kunstleve, R. W., Jiang, J. S., Kuszewski, J., Nilges, J. M., Pannu, N. S., Read, R. J., Rice, L. M., Simonson, T., and Warren, G. L. (1998) *Acta Crystallogr. D54*, 905−921.
31. Russel, A., and Cambillau, C. (1991) *Turbo Frodo*, Silicon Graphics, Mountain View, CA.
32. Collaborative Computational Project Number 4 (1994) *Acta Crystallogr. D50*, 760−763.
33. Roy, A. V., Brower, M. E., and Hayden, J. E. (1971) *Clin. Chem. 17*, 1093−1102.
34. LaCount, M. W., Handy, G., and Lebioda, L. (1998) *J. Biol. Chem. 273*, 30406−30409.
35. Kuciel, R., Bakolova, A., Mazurkiewicz, A., Biliska, A., and Ostrowski, W. (1990) *Biochem. Int. 22*, 329−334.
36. Porvari, K. S., Herrala, A. M., Kurkela, R. M., Taavitsainen, P. A., Lindqvist, Y., Schneider, G., and Vihko, P. T. (1994) *J. Biol. Chem. 269*, 22642−22646.
37. Beers, S., Schwender, C., Loughney, D., Malloy, E., Dermarest, K., and Jordan, J. (1996) *Bioorg. Med. Chem. 4*, 1693−1701.
38. Yao, Z. J., Ye, B., Wu, Z. W., Wang, S., Wu, L., Zheng, Z. Y., and Burke, T. R., Jr. (1998) *Bioorg. Med. Chem. 6*, 1799−1810.
39. Wallace, A. C., Laskowski, R. A., and Thornton J. M. (1995) *Protein Eng. 8*, 127−134.

BI0265067